Multimodal assessment of mechanically induced transformation and damage in TRIP steels using X-ray nanotomography and pencil-beam diffraction tomography

Toda, Hiroyuki
Department of Mechanical Engineering, Kyushu University

Koga, Chiharu
Department of Mechanical Engineering, Kyushu University

Hirayama, Kyosuke
Department of Materials Science and Engineering, Kyoto University

Takeuchi, Akihisa
Japan Synchrotron Radiation Research Institute

他

出版情報：Acta Materialia. 281, pp.120412-, 2024-12-01. Elsevier
バージョン：

Acta Materialia 281 (2024) 120412

Contents lists available at ScienceDirect

Acta Materialia

journal homepage: www.elsevier.com/locate/actamat

Full length article

Multimodal assessment of mechanically induced transformation and damage in TRIP steels using X-ray nanotomography and pencil-beam diffraction tomography

Hiroyuki Toda [a,*], Chiharu Koga [a], Kyosuke Hirayama [b], Akihisa Takeuchi [c], Masayuki Uesugi [c], Kyohei Ishikawa [d], Takafumi Yokoyama [d], Hiro Fujihara [a]

[a] Department of Mechanical Engineering, Kyushu University, 744, Motooka, Nishi ward, Fukuoka city, FUKUOKA 819-0395, Japan
[b] Department of Materials Science and Engineering, Kyoto University, Yoshida Honmachi, Sakyo-ku, KYOTO 606-8501, Japan
[c] Japan Synchrotron Radiation Research Institute, 1-1-1, Kouto, Sayo-cho, Sayo-gun, HYOGO 679-5198, Japan
[d] Steel Research Laboratories, Nippon Steel, 20-1, Shintomi, Futtsu, CHIBA 293-8511, Japan

ARTICLE INFO

Keywords:
Mechanically induced transformation
C-Mn-Si steel
Nano-tomography
X-ray diffraction
Damage
Mechanical driving force

ABSTRACT

A comprehensive multimodal measurement environment integrating X-ray computed tomography (CT) and special X-ray diffraction (XRD) using a collimated beam has been developed and was applied for the first time to investigate martensitic transformation and damage behaviour in transformation-induced plasticity (TRIP) steels. The transformation and damage behaviour of numerous γ grains were analysed individually to understand the behaviours and to identify the factors controlling these processes.

A transition was observed from a stress-assisted transformation in the early loading phase, controlled by mechanical driving forces, to a strain-induced transformation controlled by dislocation density. A characteristic reversal in the transformation rate was observed whereby γ grains with a crystallographic orientation that initially undergo rapid transformation due to high mechanical driving force underwent a sudden deceleration of transformation. Conversely, γ grains with an orientation that initially underwent gradual transformation rapidly completed transformation. The preceding hard phase inhibited the transformation of neighbouring γ grains through the triple effects of reducing stress triaxiality, relaxing stresses and constraining plastic deformation.

The growth of pre-existing voids was modest, and material damage was dominated by voids that were newly formed during deformation from α′ grains. The initiation and progress of damage were influenced by the combined effects of the γ grain morphology and their interaction with surrounding α′ grains. The complexity of the local morphology governed the martensitic transformation and damage behaviour, and geometrical parameters were identified as highly sensitive indicators for describing this phenomenon. Finally, industrial measures to design damage-resistant TRIP steels based on these research findings are discussed.

1. Introduction

TRIP steels are duplex-phase steels consisting of metastable austenite (γ), ferrite (α) and bainite. Under external forces, the γ phase transforms into martensite (α′), which is known for its high strength. The dispersion of these high-strength phases and the internal stresses resulting from the volumetric expansion during martensitic transformation increases the strength of TRIP steels. At the same time, these factors promote work hardening and reduce local deformation, resulting in enhanced ductility of the material. This results in an excellent strength–ductility balance. [1] For example low carbon C-Mn-Si steels with tensile strengths of approximately 1000 MPa have been reported to have in situ strengths of around 800 MPa and 800–1200 MPa for the α matrix and γ phase, respectively [2]. In contrast, the newly formed α′ phase under loading shows a very high in situ strength of 2300–2800 MPa. This is well above the strength of martensite typically found in dual-phase steels (1000–2000 MPa) [3,4,5].

To take advantage of the excellent strength–ductility balance of TRIP steels, martensitic transformation must progress gradually as the material is deformed. The stability of the γ phase is important for this process. This stability depends on several factors, such as the morphology of the dispersed phase, its interaction with the surrounding microstructure,

* Corresponding author.

https://doi.org/10.1016/j.actamat.2024.120412
Received 1 February 2024; Received in revised form 22 August 2024; Accepted 13 September 2024
Available online 19 September 2024

crystallographic orientation, dislocation density and chemical composition [6]. The influence of each of these factors has been extensively studied [7-22]. In particular, the influence of alloying elements such as carbon, manganese and silicon is well understood. For example, although the segregation of manganese into the γ phase improves its stability [23-26], excessive segregation can reduce the volume fraction and carbon content of the γ phase, which, in turn, leads to reduced ductility [27]. Conversely, silicon inhibits the formation of carbides and increases the stability of the γ phase by enriching the solid solution carbon of the γ phase [28]. Increasing the γ-phase volume fraction also reduces the stability of the γ phase by reducing the average carbon concentration [29]. Tsuchida et al. [15] found that the needle-like γ phase is more stable than the massive γ phase, which is attributed to the strain differences between the α and γ phases due to the higher carbon concentration. Thus, the influence of microstructural morphology on martensitic transformation behaviour is often closely linked to the chemical composition.

In addition, the distribution of stress and strain, which are influenced by the different deformation resistances of the constituent phases, varies with the shape, size, density and spatial distribution of the individual dispersed phases, their location, and macro and micro stress states. All these elements collectively affect the martensitic transformation rate [13,16,18]. For example, Zhang et al. [13] and Tirumalasetty et al. [16] have shown the effect of the matrix microstructure near the γ phase and its size on the stability of the γ phase. However, even in a hypothetical scenario where a TRIP steel has a perfectly uniform size, shape, spatial distribution and alloying element concentrations, as well as a perfectly random crystallographic orientation distribution, not all γ grains will transform simultaneously and instantaneously. In fact, research has shown that in situ observation of tensile tests using X-ray CT has shown that the martensitic transformation of each γ-phase grain occurs gradually to different degrees and that the rate of transformation varies from grain to grain [30]. This is due to the considerable strength difference between the α′ phase and the combination of the γ phase and matrix α phase. Moreover, the γ-phase grains that transform before the other γ-phase grains due to their crystallographic orientation or other factors have a considerable influence on the transformation behaviour of the surrounding γ-phase grains. Therefore, even if the aspects and properties of individual γ-phase grains are evaluated, the nature of their phase stability cannot be understood without examining the effects of the sequential martensitic transformation of closely interacting γ-phase grains. It goes without saying that such time-evolution behaviour cannot be approached by evaluations solely based on the average values of various factors related to the stability of the γ phase.

In addition to accurately characterizing the shape, size and spatial distribution of the dispersed phases, X-ray CT and special XRD techniques allow direct observation of grain-to-grain interactions and various time-evolution behaviours [31]. Jimenez et al. [11] and Blonde et al. [17] have used the 3D-XRD method [31,32] to measure the three-dimensional (3D) geometry and crystallographic orientation of the γ-phase grains. Their research has yielded valuable insights, including data on the carbon content and grain size of the individual γ-phase grains and the relationship between crystallographic orientation and martensitic transformation behaviour. However, the diffraction spots obtained by XRD are blurred due to plastic deformation of the material, which limits their measurements to no-load (i.e. transformation during cooling) or low-load scenarios with up to 2% applied strain. Consequently, their studies did not evaluate the sequential martensitic transformation behaviour and its interference effects with the surrounding microstructure.

Previous studies have analysed the deformation, damage and fracture of duplex microstructures using the X-ray CT method, as it is not affected by plastic deformation [30,33-35]. In particular, in a previous study, multimodal measurements combining X-ray CT and XRD were applied to analyse the martensitic transformation in TRIP steels. In this study, the four-dimensional (4D) microstructural morphology of the γ phase was captured using X-ray CT, and the crystallographic orientation was mapped in 4D by a special XRD technique known as pencil beam XRD in which the sample was rotated while performing raster scanning with a collimated X-ray beam [30]. Initially, the 3D crystallographic orientation information of the γ phase was obtained by pencil beam XRD under no-load conditions. Subsequently, phase-contrast imaging-type X-ray CT was used to obtain and correlate high-resolution images of individual γ-phase grains and their extinction behaviour during transformation. Meanwhile, pencil beam XRD measurements were performed on a separate specimen consecutively from no load to specimen rupture to obtain a coarse 4D crystallographic orientation distribution over time. By synthesising this information, the local martensitic transformation behaviour, including the interactions between grains of the γ phase, was assessed as a time-evolution behaviour. As a result, the effects of factors such as crystallographic orientation, grain size and dislocation density on the transformation rate of individual γ-phase grains was quantitatively evaluated in terms of transformation mechanisms and the driving forces behind these transformations [30]. However, at the time of this experiment, the technology did not allow the repeated alternation between high-resolution imaging-type X-ray CT observations and precise pencil beam XRD measurements on a single specimen. Consequently, the experiment was only able to partially integrate these two techniques, as previously described. As a result, only rudimentary results were obtained regarding the interference effects between adjacent different phase microstructures (Fig. 11 in reference [30]). The data obtained, albeit spatially coarse, did provide initial examples suggesting suppression of deformation and delayed martensitic transformation of the γ-phase grains by adjacent α′-phase grains.

The authors have recently made significant improvements to the techniques previously described, enabling comprehensive multimodal measurements combining X-ray CT and pencil beam XRD. In this study, these enhanced methods are applied to the same TRIP steel as in the previous report to analyse in more detail the transformation behaviour of individual γ-phase grains, including their interactions with neighbouring grains. The damage behaviour of individual γ-phase grains, which could not be accurately analysed in the previous study, is also being analysed. The ultimate aim is to identify the key factors that influence the transformation and damage behaviour of γ-phase grains. This research aims to provide insights for the design of TRIP steel microstructures with high resistance to damage.

2. Experimental and analytical methods

2.1. Test and test specimens

The sample is a low-carbon C-Mn-Si multi-phase steel with 0.1% C, 5% Mn and 2% Si in mass %. A cold-rolled steel plate was subjected to three heat treatment steps to obtain various shapes of retained austenite: 1) intercritical annealing at 973 K for 400 h, followed by air cooling to room temperature, 2) austenitising at 1173 K for 1800s, followed by furnace cooling to room temperature, 3) intercritical annealing at 933 K for 100 h, followed by air cooling to room temperature. The steel used consisted of γ phase and α phase, with a volume fraction of γ phase of 26.9%, average γ- and α-phase grain sizes of 1.3 and 3.3 μm respectively, and their standard deviations of 0.86 and 4.44 respectively. The average diameter of the γ-phase grains is 3.5 μm. The elemental concentration of the γ phase measured by electron probe microanalysis (JEOL JXA-8500F was used: the spatial resolution of the measurement is 1 μm) was 0.45% C, 9.10% Mn and 2.00% Si. Using the empirical formula by Kaar et al., the martensite start (M_S) temperature point is calculated to be 11.9 °C [19]. According to Samek et al., the M_S^σ point (the maximum temperature transformation is induced by stress application) for low-carbon C-Mn-Si multi-phase steels ranges between −5 °C and 20 °C and is less affected by the concentration of alloying elements [18]. Therefore, the specimens have moderate γ-phase stability for C-Mn-Si multiphase steels. The initial γ-phase distribution is shown in Fig. S1 (a)

A tensile specimen with a thickness of 1.4 mm was extracted from a rolled plate using electrical discharge machining in the longitudinal–-transverse direction, and its rectangular gauge section was electro-polished to form a cylindrical shape with a diameter of approximately 0.1 mm. To prevent the deformation of the specimen during electro-polishing and its subsequent mounting in the materials testing machine, the specimen was fitted with a reinforcing jig made of SUS 304 stainless steel after electrical discharge machining. This jig was carefully removed after the specimen was mounted into the materials testing machine.

2.2. Synchrotron radiation experiments

The experimental setups for projection- and imaging-types X-ray CT and pencil beam XRD, as shown in Fig. 1, were installed in the SPring-8 beamline BL20XU. The three setups can be interchanged in a few minutes by moving the detector, Fresnel zone plates (FZPs), condenser zone plate (CZP) and object scanning assembly in or out of the optical axis. The use of a high-precision, fast-rotating air-bearing stage and an experimental sequence that allows precise alignment of the imaging-type X-ray CT data with the pencil beam XRD data has enabled comprehensive multimodal measurements. Previously, the high-precision rotation stage for imaging-type X-ray CT and the high-speed sample rotation stage for pencil beam XRD, as cited in the literature [35], achieved rotational accuracies and speeds of 0.15 μm/10°/s and 1 μm/40°/s, respectively. In contrast, the sample rotation stage used in this study achieved a significant enhancement with a capability of 0.15 μm/7200°/s. This represents a dramatic increase in speed while maintaining the high precision required for the imaging of imaging-type X-ray CT.

After observing the overall image with projection X-ray CT, a total of seven measurements, including the unloaded state, were conducted in the order of pencil beam XRD and imaging-type X-ray CT, with the displacement increased by a predetermined amount. In the small materials testing machine used, a polymer cylinder was used as a load frame to prevent the attenuation of X-rays. In addition, two holes were drilled in the polymer cylinder for the removal of the specimen

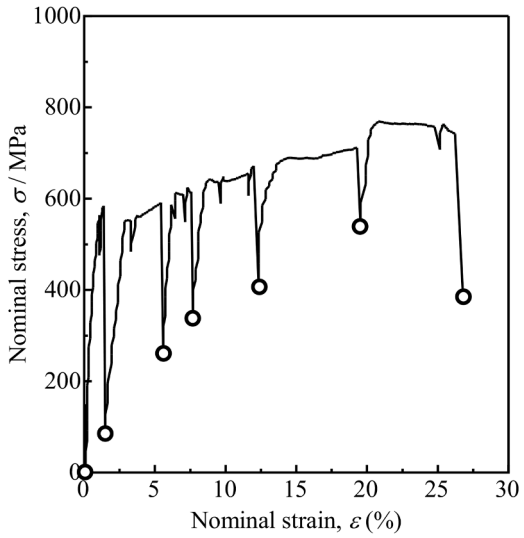

Fig. 2. Graph shows the nominal stress and strain curve recorded during the *in-situ* tensile test conducted at the synchrotron radiation facility. Circles denote the levels of applied strain at which X-ray computed tomography observations and X-ray diffraction measurements were performed.

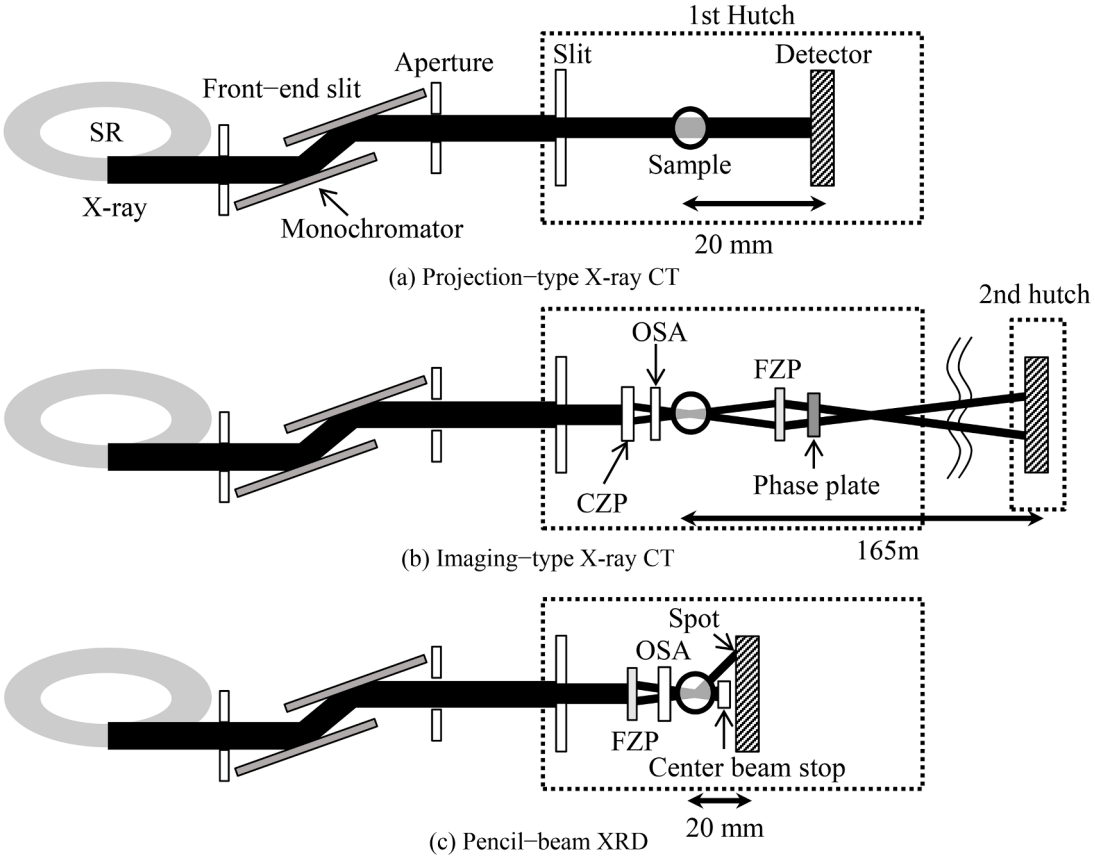

Fig. 1. A schematic illustration of the three experimental set-ups for the comprehensive multimodal measurement environment integrating X-ray computed tomography and specialised X-ray diffraction measurements, conducted using a collimated X-ray beam.

reinforcement jig. The stress–strain diagram in Fig. 2, which was measured during the synchrotron radiation experiment, shows that due to the low stiffness of the load frame, unloading occurs each time it is observed and measured. This unloading is expected to have a small influence on the transformation and damage behaviour of the material. Image blur during pencil beam XRD measurements, which is mainly caused by this unloading, is measured at a maximum of 0.14 μm. The effect of this blurring was also experimentally measured and evaluated, as described below.

The imaging-type X-ray CT used in this study was a Zernike phase contrast X-ray microscope consisting of a Köhler illumination system using a CZP, an FZP with a diameter of 310 μm and an outermost bandwidth of 100 nm, and a phase plate inserted in the backward lateral focal plane. The detection system consisted of an ORCA Flush 4.0 Hamamatsu Photonics CMOS camera with 4 million pixels and a pixel size of 6.5 μm. In addition, a 10-fold optical lens and a scintillator (200 μm thick LuAG: $Lu_3Al_5O_{12}$:Ce^{+}) were placed 165 m from the sample. The X-ray energy utilised was 30 keV. A total of 3600 projected images were captured over a 180° rotation, each with an exposure time of 1 s. The actual pixel size measured in the 3D image was 65 nm and the spatial resolution was approximately 150 nm. To confirm the positions of the grain boundaries in the γ phase, the tensile specimen was not fractured, and the measurement was terminated at an applied strain of 26.8%.

For the pencil beam XRD, an X-ray pencil beam with a diameter of 2.5 μm (full width at half maximum) was used, formed by an FZP with a diameter of 310 μm and an outermost bandwidth of 150 nm. The X-ray pencil beam was raster-scanned across 20 vertical and 27 horizontal layers in 3-μm steps, and at each beam position, the specimen was rotated 180° in 1° increments, resulting in a total of 98,279 X-ray diffraction patterns per loading step. The same CMOS detector as used in the X-ray CT was used with a 10-fold optical lens and a scintillator (20-μm thick P43 (Gd_2O_2S:Tb_{+})), positioned 25 mm from the sample, with an X-ray energy of 37.7 keV and an exposure time of 150 ms. Prior to the main measurement, X-ray diffraction patterns of 20 vertical layers, corresponding to the rightmost column in the raster scan, were obtained separately for validation processes, and then the main raster scan measurement was conducted. A comparison of the two results showed that the positional accuracy of the lateral movement of the CMOS camera, which is the least accurate in the pencil beam XRD measurement system, was better than 0.6 μm. This accuracy is less than 5% of the spatial resolution of the pencil beam XRD measurement, indicating that blurring due to the raster scan operation of the detector or specimen relaxation during the scan does not affect measurement accuracy.

2.3. Image analysis

2.3.1. Imaging-type X-ray CT

For noise reduction, a 5 × 5 × 5 voxel median filtering technique was applied to the 3D images. Adaptive thresholding segmentation [36] was applied to address artifacts caused by region-of-interest imaging. The required segmentation sensitivity, *t*-value, and kernel size, *K*, which is the size of the local region of interest, were determined so that the γ-phase volume fraction obtained from the imaging-type X-ray CT and pencil beam XRD experiments matched. Note that *K* was set to 4 μm.

Watershed processing was then applied to the 3D image before loading [31] to determine the grain boundary positions of the γ phase. First, the H-minima transform [31] was applied to the images after the distance transform [31] to avoid oversegmentation caused by the watershed processing. Then the watershed process was applied. In this case, the H value of the H-minima transform was set to 5. The 3D grain boundary images of the γ-phase grain boundaries at each loading stage were obtained by multiplying the initial 3D grain boundary images obtained at the unloaded stage through this method with the affine transformation matrix obtained by registering the 3D images at each loading stage. To ensure that the number of austenite grain boundaries counted in the 2D austenite image in the unloaded EBSD image is the same as that obtained by watershed processing of the 3D X-ray CT images, which was displayed on the 2D virtual section in a form that can be compared with the EBSD data, the H value has been adjusted to correct for issues of oversegmentation and undersegmentation. An example of EBSD data is available in supplementary material as Fig. S2 for reference.

Various size and shape parameters were used to quantitatively assess the size and shape of the individual γ-phase grains separated using the abovementioned process. Specifically, 7 size parameters and 12 shape parameters were used, excluding those related to the mean curvature, which are listed in Table S1 in the literature [37].

The parameters used included spherical equivalent diameter, geodisperse distance, volume, surface area, angle between the principal axes and direction of loading, as well as 14 parameters beginning with *o, p* and *f*. *o* is the aspect ratio defined by the three principal axes. *p* is the ratio of the first, second, third and fourth moment invariants, which represent the position of the centre of gravity and its deviation, skewness and kurtosis, etc. *f* is the deviation from a sphere or cube. Therefore simple and conventional parameters such as γ grain size are also included in the analysis.

Here is a brief explanation of the meaning of the two selected parameters. A 3D object can be described by a gray function $f(x, y, z)$, where x, y, z are the coordinates in the 3D world. For similarity, we can only consider binary image. That is $f(x, y, z)=1$, when inside voxels belonging to an object and 0 in free space. The 3D moments of order $n = p + q + r$, are defined as follows:

$$m_{pqr} = \int\int\int x^p y^q z^r f(x,y,z)dxdydz \tag{1}$$

for $p, q, r = 0, 1, 2, \ldots$. Adapting this to image with voxels $f(x, y, z)$, the image moments m_{pqr} are calculated by:

$$m_{pqr} = \sum_x \sum_y \sum_z x^p y^q z^r f(x,y,z) \tag{2}$$

For $n = 2$, the second-order define the variance, which describes the deviation from the center:

$$p_7 = \left(m_{200} * m_{020} * m_{002} - m_{002} * m_{110}^2 - m_{020} * m_{101}^2 - m_{200} * m_{011}^2 + 2 * m_{100} * m_{101} * m_{011}\right) / m_{000}^4 \tag{3}$$

For $n = 3$, the third-order define the skewness, which is a measure of the lopsidedness of the distribution; any symmetric distribution will have a third central moment, if defined, of zero.

$$p_8 = \left(m_{300}^2 + m_{030}^2 + m_{003}^2 + 3m_{120}^2 + 3m_{102}^2 + 3m_{012}^2 + 3m_{021}^2 + 3m_{210}^2 + 3m_{210}^2 + 6m_{111}^2\right) / m_{000}^5 \tag{4}$$

In addition, voids were segmented from the filtered 3D images using a specific segmentation technique. The position of their centre of gravity, sphere equivalent diameter, surface area and volume were then measured. For this analysis, features with a volume of 27 voxels or more were taken as voids, considering the effective spatial resolution of the imaging technique. The 3D image captured in the final loading stage showed 105 voids. The physical displacement of each void was traced backward in time from the final loading stage to the pre-loading stage. This retrospective analysis helped to determine the extent of strain responsible for the formation of each void and the initial microstructure present at the point of origin of each void.

2.3.2. Pencil beam XRD

After binarisation of the X-ray diffraction images, structures occupying an area smaller than 9 pixels were considered as noise and excluded from the analysis. There were approximately 36 million diffraction spots in the filtered X-ray diffraction images in the initial unloaded state. Of these, approximately 2400,000 were located within

21 μm of the Debye rings of the γ-phase planes (111), (200) and (220) on the detector plane. The remaining diffraction spots were either attributed to image noise or identified as double diffraction. All diffraction spots were traced in chronological order from the no-load state [31], and all identical diffraction spots were matched.

To calculate the γ phase volume fraction at each loading stage, the integrated intensity of the diffraction peaks at the respective lattice planes of α and γ was obtained. The intensities of the diffraction spots were integrated along the Debye rings in all X-ray diffraction images and summed to generate a line profile representing the diffraction intensities. This profile underwent Gaussian fitting to obtain the integrated intensity of the diffraction peak at each lattice plane for both the α and γ phases, and the phase fraction was calculated assuming a proportional relationship between the intensity of the diffraction peaks and the volume fraction of each phase [38]. In the data analysis process, the data are corrected in accordance with ASTM E975–22.

In this study, a raster scan covering a 60-μm long and 81-μm wide area was conducted using a 2.5-μm diameter collimated X-ray beam. This approach was employed to obtain diffraction spots from γ-phase grains with an average equivalent sphere diameter of 3.5 μm and a maximum diameter of 6.4 μm. Thus, diffraction spots from the same γ-phase grains were obtained at several adjacent beam positions on a single diffraction image. In the actual measurements, diffraction spots from the same γ-phase grains were observed up to three times in the longitudinal direction and up to four times in the transverse direction. To systematically analyse these observations, a clustering process was performed to label the same diffraction spots from the same γ-phase grains together [31,33]. Specifically, diffraction spots that appeared at the same sample rotation angle ω and whose centroids were within a 5-pixel radius of each other on the detector coordinates were considered as a cluster of diffraction spots. 3D clustering [33] was also employed to cluster diffraction spots with a sample rotation angle of $\omega \pm 3^\circ$ This allowed the superimposition of optical axis projection images of individual γ-phase grains, which were visualised in 3D through X-ray CT, onto the clusters of diffraction spots obtained from pencil beam XRD measurements. Such superimposition [31,33] facilitated the precise alignment of these two sets of data. Twenty residual γ-phase grains with a larger grain size (mean sphere equivalent diameter 5.2 μm) were selected for confirmation, and the discrepancy between X-ray CT and pencil beam XRD images was found to be less than 1 μm, which is less than 8% of the spatial resolution of the pencil beam XRD measurement. This minimal discrepancy indicates that potential misalignments between the X-ray CT and pencil beam XRD images, as well as any blurring due to the relaxation behaviour of the specimen during measurement, do not affect the measurement accuracy.

For all clustered diffraction spots, scattering vectors were calculated, taking into account the sample rotation [31,33]. If a given γ-phase grain and two or more of its diffraction spots are correctly associated, the crystallographic orientation of the grain can be accurately calculated. However, if there are γ-phase grains of similar shape and size in the projected image along the optical axis, there is a risk of incorrect assignment of γ-phase grains to diffraction spot clusters. Therefore, after calculating the crystallographic orientation using all diffraction spot pairs mapped to a particular γ-phase grain, the calculated crystallographic orientation solutions that clustered within an 1° range in 3D orientation space were considered as the crystallographic orientation solution group. The crystallographic orientation of the solution group with the highest number of clustered solutions was selected as the crystallographic orientation for that particular γ-phase grain.

The half-widths of the peaks of diffraction spots in the {111}, {200} and {220} planes associated with a single γ-phase grain were measured, and the average dislocation density for each grain was calculated using the modified Williamson–Hall method [39].

3. Experimental results

3.1. Martensitic transformation behaviour

3.1.1. Influence of γ-phase grain size and shape

Fig. 3 shows the 3D morphology of all 170 γ-phase grains for which the martensitic transformation behaviour could be traced, showing how it changes with external loading. For reference, Fig. S1 shows the change in the distribution of γ phase on a 2D virtual cross section. The orientation of the γ-phase grains corresponds to the colours shown in the inverse pole figure. The γ and α phases have sufficient density differences to allow segmentation, but the density difference between the α and α′ phases is close to the density resolution limit of the measurement system. This made segmentation challenging, although the presence of these phases could be confirmed on virtual cross-sections. Therefore, only the γ phase is shown in Fig. 3. The figure shows that most γ-phase grains are oriented in the ⟨111⟩ direction. In addition, almost all γ-phase grains are three-dimensionally connected prior to loading. At an applied strain of 1.5%, martensitic transformation is already well advanced, and the γ-phase grains disappear. This transformation becomes more pronounced at 5.6% applied strain, with a significant number of γ-phase grains completing the martensitic transformation. A small number of grains persist up to an applied strain of 19.5%, but even these have completed the transformation by 26.8% applied strain.

Initially, the γ-phase grains were classified into three shapes: needle, lump and plate [15], as per the criteria outlined in the literature. This classification was based on the diameters in the principal axial directions, denoted as o_1, o_2 and o_3 ($o_1 \geq o_2 \geq o_3$). Needle, lump and plate grains were defined as $o_2/o_1 \geq 0.5$, $o_2/o_1 < 0.5$ and $o_3/o_2 < 0.5$, and $o_2/o_1 < 0.5$ and $o_3/o_2 \geq 0.5$, respectively. This resulted in a total of 170 γ-phase grains being classified into 28 needle, 81 lump and 61 plate grains. Fig. 4(a) shows the martensitic transformation behaviour of the γ-phase grains for each shape. This simplified classification shows no difference in the transformation behaviour among the different shapes. Fig. 4(a) also shows typical needle, lump and plate-like γ-phase grains. However, given the complex geometry of the γ-phase grains, it became evident that such a simplistic morphological classification might not be adequate. Therefore, a more detailed morphology assessment was carried out.

The size and shape parameters defined in Section 2.3.1 were calculated for γ-phase grains that had undergone only 10% transformation of their initial volume at a given applied strain. The applied strain is denoted as $\varepsilon^{10\%}_{\text{trans.}}$ and the mean value of each parameter is denoted as $x_{\varepsilon^{10\%}_{\text{trans.}}}$. The mean values of each parameter when $\varepsilon^{10\%}_{\text{trans.}}$ was 1.5% and 5.6% were determined, and their ratio ($x_{1.5\%}/x_{5.6\%}$) is shown in Fig. 5 (a). It can be seen that p_7, which represents the deviation of the voxel distribution, and p_8, which represents the skewness of the voxel distribution, have a high sensitivity to strain.

For both parameters, a larger $x_{1.5\%}/x_{5.6\%}$ ratio indicates a more complex particle shape. Fig. 4(b) shows the relationship between the size of p_7 and the martensitic transformation behaviour, focusing on cases where the $x_{1.5\%}/x_{5.6\%}$ value of p_7 is larger. It can be seen that when p_7 is greater than its median, the volume of the γ-phase grains decreases more rapidly than when p_7 is less than its median. This effect is particularly clear at applied strains above 5.6%.

3.1.2. Interference effects of γ-phase grains

Fig. 6 shows the effect of the γ-phase volume fraction on the martensitic transformation of the γ-phase grains being studied. In this case, 'neighbourhood' was defined as the area within a radius of 7 μm from the centre of gravity of the γ-phase grains. When the volume fraction of the γ phase in the vicinity is lower than 10%, the transformation occurs rapidly. This effect is evident over a wide range of applied strains. As the γ-phase volume fraction increases from 10% to 15% and above 15%, the transformation rate decreases noticeably.

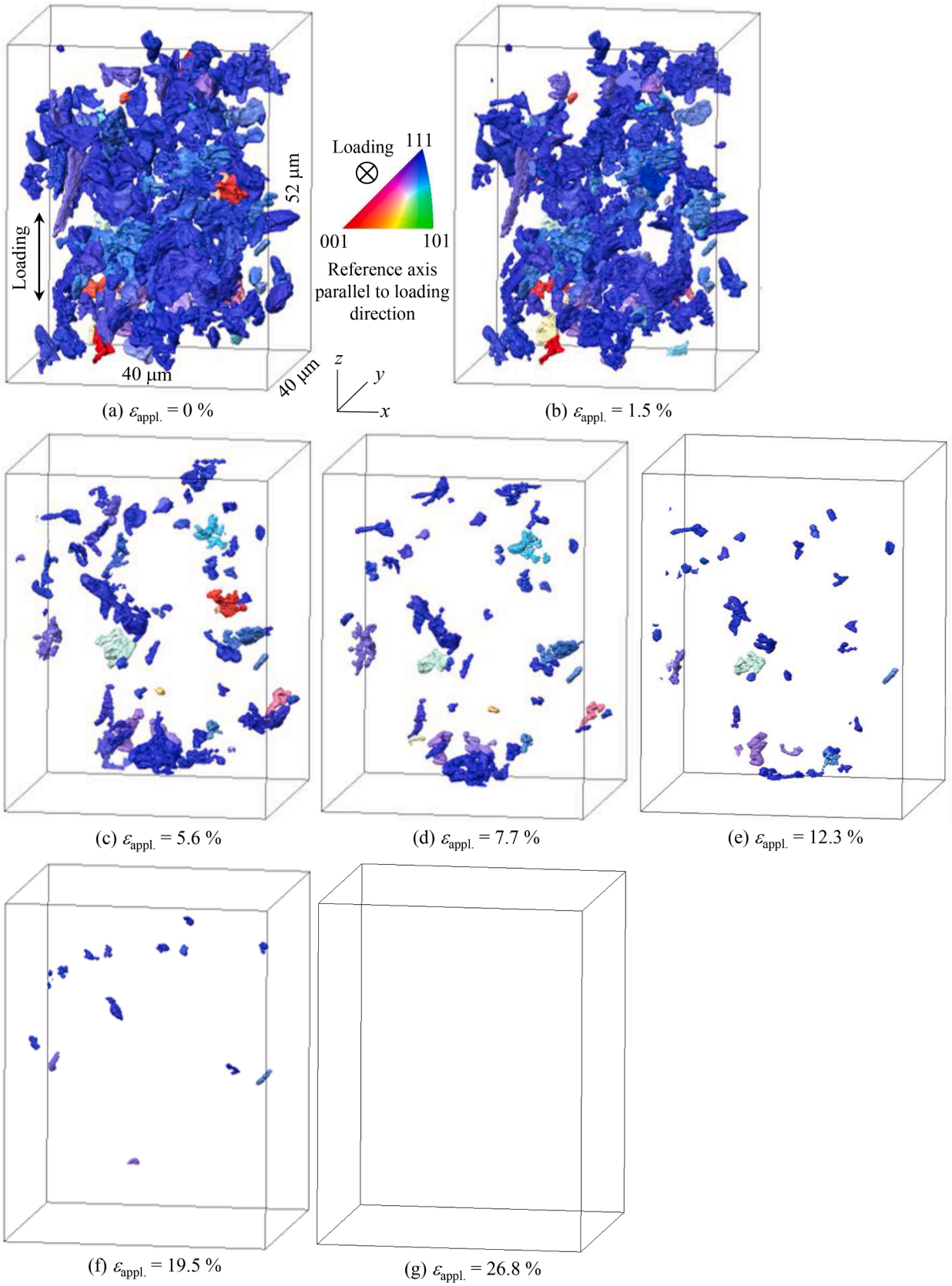

Fig. 3. 3D morphologies and crystallographic orientations of all 170 grains that were located in the 40 × 40 × 52 mm region of interest. The colour code in the 3D images corresponds to the [001] inverse pole figure shown in (a).

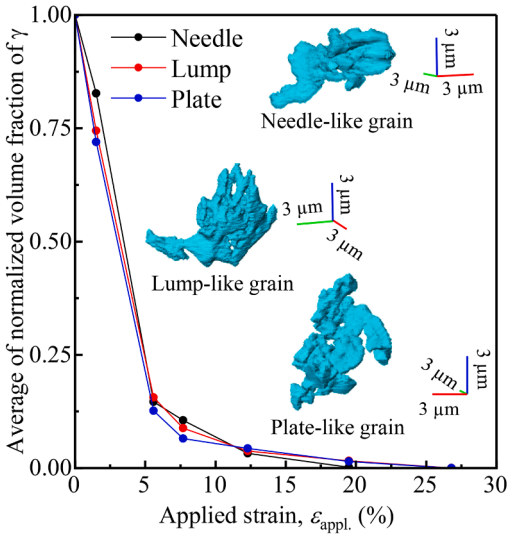

(a) Effects of simplified geometries of γ phase grains on martensitic transformation rate

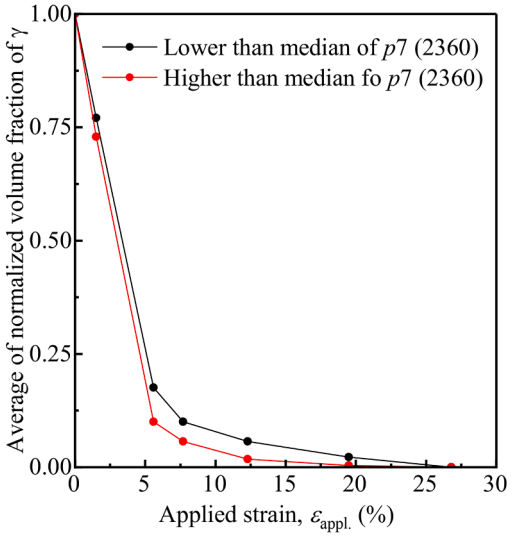

(b) The effects of local complex shapes and irregularities defined by the deviation of the 3D pixel spatial distribution, p_7

Fig. 4. The martensitic transformation behaviour of (a) the γ-phase grains for each simplified shape category: needle-, lump- and plate-like γ-phase grains, and (b) those classified by the size of the deviation of the voxel spatial distribution, denoted as p_7.

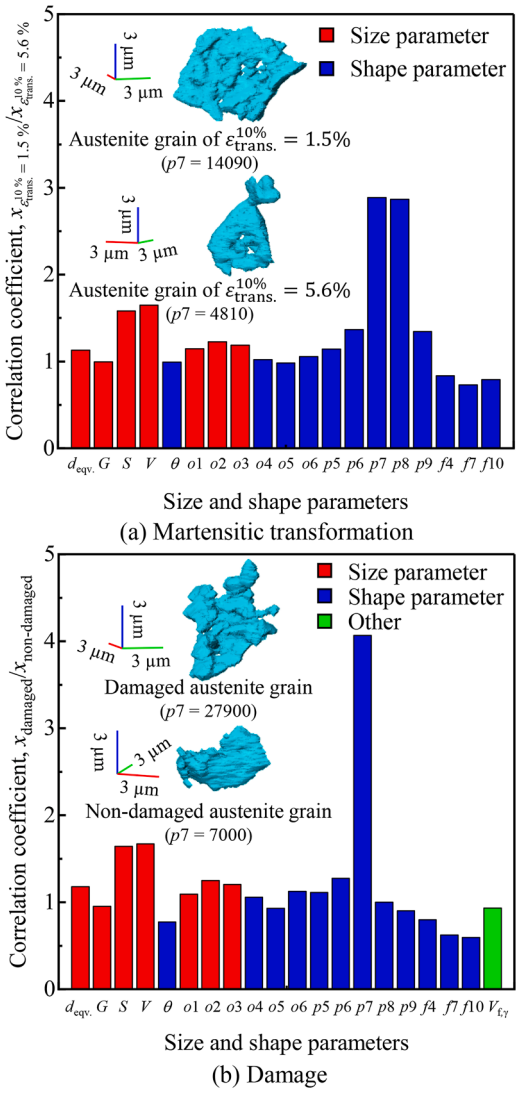

Fig. 5. (b) Correlation coefficients between design variables for the size and shape of γ-phase grains for (a) martensitic transformation and (b) damage. The mean value of each parameter denoted as $x_{\varepsilon^{10\%}_{trans.}}$ is calculated in (a) at an applied strain of $\varepsilon^{10\%}_{trans.}$ at which only 10% of the initial volume of a γ-phase grain is transformed to take ratios between the applied strain levels of 1.5% and 5.6%. In (b), the size parameter and shape parameters were averaged for undamaged and damaged γ-phase grains after transformation to facilitate comparison between them.

3.1.3. *Effects of crystallographic factors*

In TRIP steel rolled plates, the α phase has a {111}<110> preferred orientation, whereas the γ phase has a {110}<111> preferred orientation. Some γ phases are also oriented in the {110}<001> direction [40]. The transformation behaviour of γ-phase grains oriented in the ⟨111⟩, ⟨110⟩ and ⟨100⟩ orientations is shown in Fig. 7(a). Fig. S3 illustrates the variability in the data by including error bars in the representation of Fig. 7(a). By assigning the γ-phase grains within 18° of each specified orientation, the distribution was found to be 151, 4, 4 and 11 grains for ⟨111⟩, ⟨110⟩, ⟨100⟩ and other orientations, respectively, with the sample used also confirming a strong {110}<111> orientation. Note that for ⟨110⟩ and ⟨100⟩ the number of grains is only four, so that observations on these orientations may lack statistical significance. During the initial phase of the deformation, γ-phase grains oriented in ⟨110⟩ and ⟨100⟩ transformed rapidly, while those oriented in the ⟨111⟩ direction and other orientations transformed at a slower rate. As in previous reports by the current authors [30], there was no accumulation of the preferential orientation due to γ-phase grain rotation during deformation, as reported by Blondé et al. [40]. This indicates that the enhanced {110}<111> orientation is attributed to the preferential transformation of γ-phase grains into orientations other than ⟨111⟩.

Fig. 7(b) shows the mechanical driving forces that facilitate stress-assisted transformation in the early stages of deformation. The mechanical driving force is the work done by the external stress. The mechanical driving force, U, is described for uniaxial tension with a tensile stress of σ_a as follows:

$$U = \frac{1}{2}\sigma_a\gamma_0 \sin 2\theta \cos\alpha \pm \sigma_a\varepsilon_0(1+\cos 2\theta) \quad (5)$$

where γ_0 is the transformation shear strain along a transformation shear direction on the habit plane, ε_0 is the dilatational strain in the direction normal to the habit plane, θ is the angle between the tensile axis and the normal to the habit plane, and α is the angle between the transformation

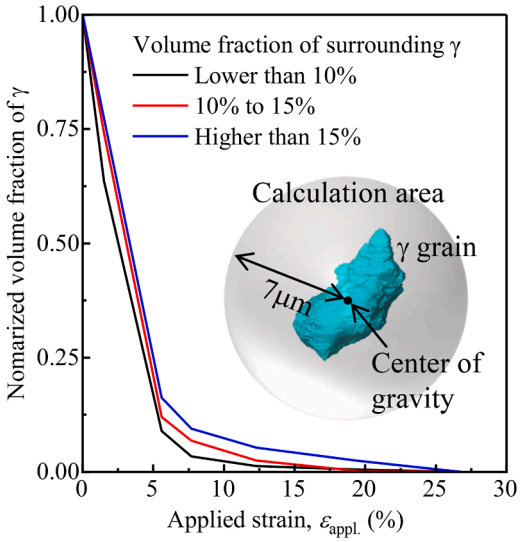

Fig. 6. Graphs show the effects of local volume fraction of γ-phase grains on their transformation behaviour. The local volume fraction was calculated in a spherical region centred at the gravity of each γ-phase grain of interest, with a radius of 7 μm.

shear direction and the maximum shear direction on the habit plane.

If the sum of the mechanical and chemical driving forces at a given temperature above the M_S point exceeds the γ-α′ free energy difference at the M_S point, martensitic transformation will occur. The γ-phase grains oriented in the ⟨110⟩ direction, which show rapid initial transformation, are found to have a high mechanical driving force. Conversely, after an applied strain of 5.6%, this trend reverses, with γ-phase grains oriented in the ⟨111⟩ direction transforming the fastest and those oriented in the ⟨110⟩ direction transforming the slowest. Fig. 7(c) shows the variation in dislocation density when the γ-phase grains are classified by their initial crystallographic orientation. The dislocation density changes for all γ-phase grains are shown in Fig. S4. For the γ-phase grains oriented in the ⟨110⟩ direction, which underwent rapid transformation in the early stages of deformation, a sharp increase in dislocation density was observed. In contrast, for grains in the ⟨111⟩ orientation, which underwent a relatively slower martensitic transformation, the increase in dislocation density was the slowest. The high initial dislocation density of the γ-phase grains oriented in the ⟨100⟩ direction is also a significant characteristic.

3.2. Damage behaviour

Fig. 8(a) shows the number of voids that occurred during each loading stage, classified by their location of occurrence. A total of 42 voids, which were present prior to loading, are shown on the left. These are considered to have occurred during rolling, and they were approximately equally distributed between γ-phase grains and α-phase grains. In contrast, a total of 105 new voids were formed during deformation, within the field of view of the imaging-type X-ray CT, and all but one of these originated from α′-phase grains after the γ-phase transformation. The changes in the average spherical equivalent diameter of the voids formed at each loading stage are shown in Fig. 8(b). The growth of the voids present prior to loading was more gradual, whereas the voids formed during deformation grew more rapidly. In particular, a tendency towards rapid growth was observed for voids formed at the final loading stage (i.e. applied strain of 26.8%). In addition, voids that occurred relatively early in the loading process, specifically at an applied strain of 7.7%, also showed significant growth. This suggests that controlling the formation and growth of voids, particularly at early stages of loading, is important.

In order to identify the factors governing the occurrence of damage, each γ-phase grain was classified according to whether it sustained damage or not, as in Fig. 5(a). For this analysis, each size parameter and shape parameter was averaged for γ-phase grains that remained undamaged after transformation and for those that were damaged after transformation. In Fig. 5(b), in addition to the size and shape parameters assessed in Fig. 5(a), the initial γ-phase volume fraction was also evaluated. As a result, Fig. 5(b) still showed a high sensitivity of the deviation parameter p_7 of the voxel spatial distribution, in relation to the occurrence of damage. The average p_7 value of the γ-phase grains that were not damaged after transformation was around 7000, whereas the damaged grains had an average p_7 value of around 30,000, showing a significant difference between the two values. This indicates that γ-phase grains with more complex shapes are more susceptible to damage. This increased susceptibility is attributed to the presence of strong stress concentration zones in the α′-phase grains after the martensitic transformation is complete.

Examples of the transformation behaviour of γ-phase grains damaged at 12.3% and 19.5% strain are shown in Figs. 9(a) and 9 (b), respectively. The growth curves of voids formed from these γ-phase grains after transformation are also shown in Fig. 9(c). The γ-phase grains shown in Figs. 9(a) and 9 (b) had already completed martensitic transformation at 7.7% strain, but the onset of damage occurred at different times. The γ-phase grains shown in Fig. 9(a), which were damaged shortly after the completion of transformation, have a large p_7 value of about 222,000 and a very distorted morphology. This value is 22.2 times higher than that of the γ-phase grains shown in Fig. 9(b), which were damaged sometime after the transformation was completed. In general, the higher the p_7 of the γ-phase grains, which transform into the α′ phase, and the lower the initial volume fraction of the surrounding γ phase, the earlier the voids tended to develop (Fig. S5). However, their effect on void growth is not always clear.

The damage behaviour of individual voids was, therefore, investigated. Examples of the transformation behaviour of γ-phase grains damaged at a strain of 26.8% and the characteristics of the surrounding γ-phase grains are shown in Figs. 10(a) and 10 (b). The growth curves of the voids formed by these γ-phase grains are shown in Fig. 10(c). The γ-phase grains shown in Figs. 10(a) and 10 (b) had completed their martensitic transformation before damage occurred. Voids were observed in the transformed γ-phase grains, particularly in areas where stress concentrations were relatively high. The γ-phase grains in Fig. 10 (a), which showed a high void growth rate, had a p_7 value of about 59,000, whereas the γ-phase grains in (b) with a low growth rate had a p_7 value of about 5000. On average, the p_7 value of γ-phase grains associated with voids is about 30,000, indicating that voids formed from complex-shaped γ-phase grains have a higher growth rate. The spherical equivalent diameters of these γ-phase grains at no load are also shown in Fig. 10. The surrounding γ-phase grains in Fig. 10(a) have a relatively small spherical equivalent diameter, whereas those in Fig. 10(b) are surrounded by coarser γ-phase grains. These γ-phase grains had all transformed to α′ by the time of void formation, thereby imposing strong deformation constraints. Conversely, there were fewer α′ grains around the γ-phase grains in Fig. 10(a), which likely facilitated plastic deformation and caused the voids to grow larger. In this way, the superposition of the effects of several factors influenced the initiation and growth of damage.

4. Discussion

4.1. Martensitic transformation behaviour

4.1.1. Interference effects between crystallographic grains

Haidemenopoulos et al. [41] showed the relationship between the stress triaxiality, $\sigma_h/\bar{\sigma}$, and the mechanical driving force as follows:

$$\frac{\partial U}{\partial \bar{\sigma}} = -0.715 - 0.3206\frac{\sigma_h}{\bar{\sigma}}, \tag{6}$$

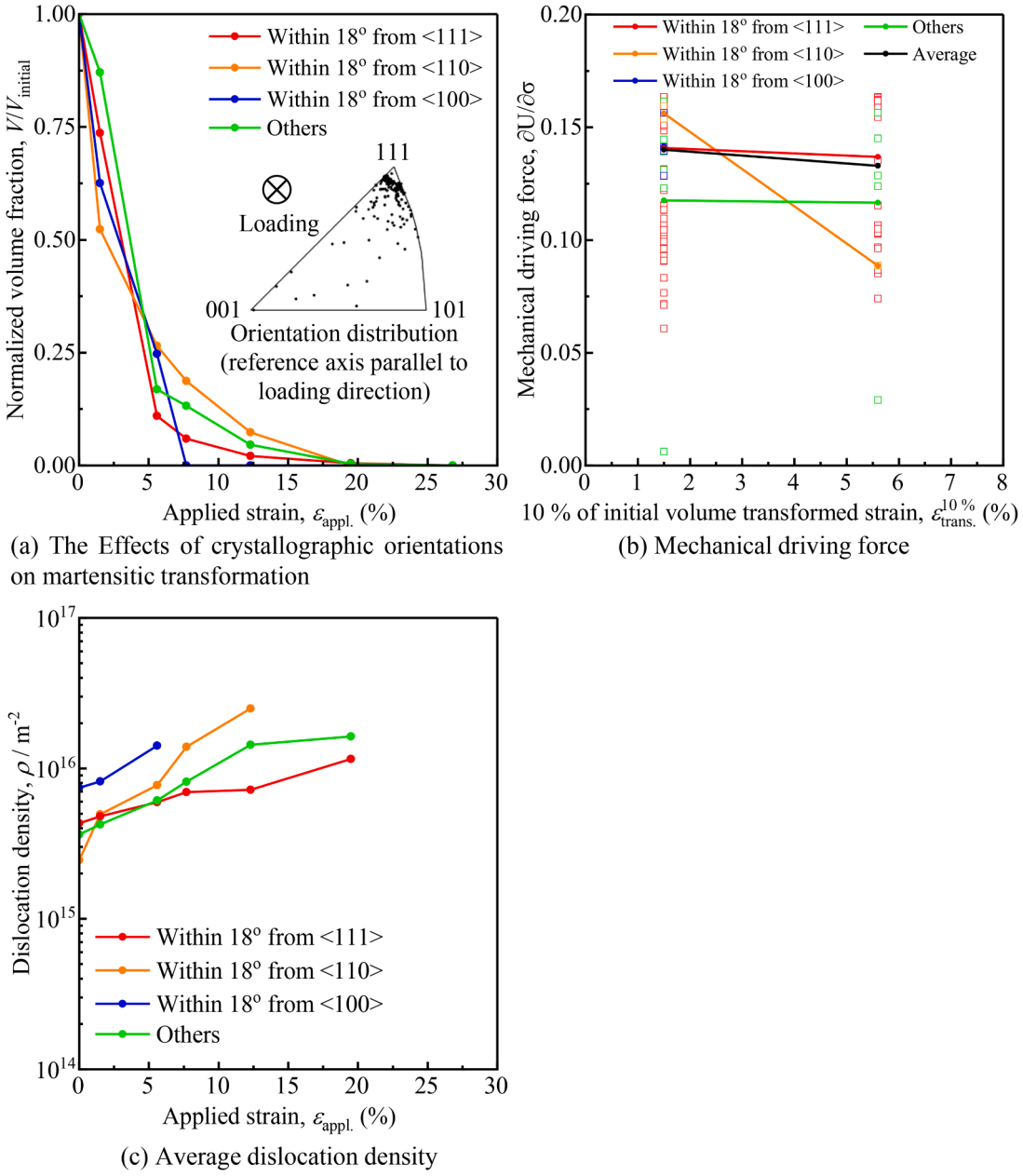

Fig. 7. The red, orange, and blue circles indicate retained austenite grains with initial grain orientations to the tensile axis within 18° of the ⟨111⟩, ⟨110⟩, and ⟨100⟩ directions, respectively (green circles denote the remaining orientations). (b) is mechanical driving force, U, for martensitic transformation expressed as $\partial U/\partial\sigma$ as a function of the nominal strain at which only 10 % of the initial volume of a γ-phase grain is transformed, and (c) is a variation in average dislocation density of γ-phase grains as a function of applied strain.

where σ_h is the hydrostatic stress and $\bar{\sigma}$ is the equivalent stress. The decrease in stress triaxiality with nucleation of the α′ phase adjacent to the γ-phase grains reduces the mechanical driving force and consequently suppresses martensitic transformation. It should be noted, however, that this simple proportionality is undermined by the preferential selection of martensitic transformations that match the orientation of the surrounding α matrix phase [42].

Haidemenopoulos et al. [43] investigated the effect of changes in stress triaxiality and the average size of γ-phase grains size in the context of the Olson–Cohen theory of heterogeneous martensite nucleation and reported that strain-induced transformation is suppressed at low stress triaxiality. In addition, isotropic expansion during martensitic transformation effectively relaxes interfacial stresses and suppresses martensitic transformation of the γ-phase grains in the vicinity [44]. The formed α′ phase behaves as a much harder phase compared to the matrix α and γ phases, as described in the introduction. It, therefore, inhibits martensitic transformation by constraining the plastic deformation of the surrounding γ-phase grains and effectively reducing the intersection of shear bands, which is the nucleus of strain-induced martensitic transformation. The effect of the preceding hard phase formation in inhibiting the martensitic transformation of the nearby γ-phase grains over a wide range of applied strains can, thus, be reasonably understood.

In the context of martensitic transformation, autocatalytic effects have been reported in the literature, where the formation of α′ plates within a single γ phase grain results in the formation of new embryos and accelerated transformation [18]. However, according to Samek et al. [18], the occurrence of the autocatalytic effect depends on the strength of the surrounding microstructure, and the effect is limited when the deformation resistance of the surrounding microstructure is high. Given

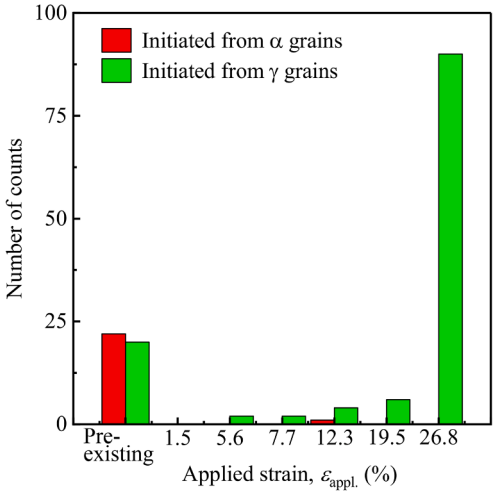

(a) Number of voids initiated at each loading stage

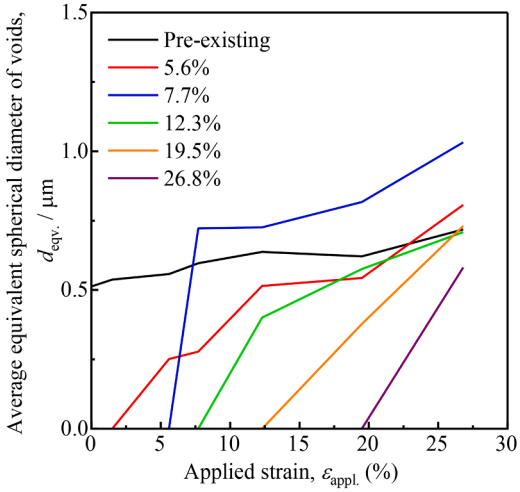

(b) Average equivalent spherical diameter of voids

Fig. 8. Graphs show (a) the number of voids initiated at each loading stage. There were 42 preexisting voids and 105 voids newly formed during deformation; and (b) changes in the average equivalent spherical diameter of voids initiated at each loading step.

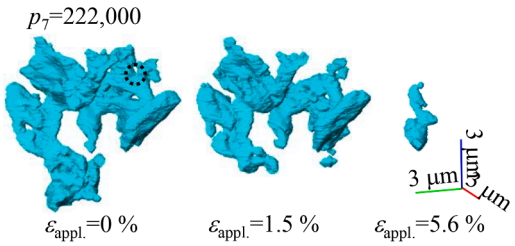

(a) Transformation behavior of a γ phase grain where a void is formed at $\varepsilon_{appl.}$ of 12.3 %

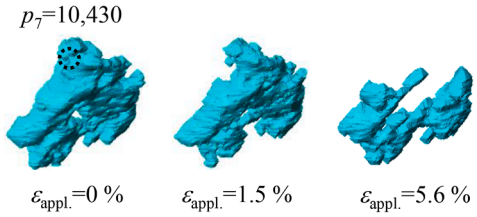

(b) Transformation behavior of a γ phase grain where a void is formed at $\varepsilon_{appl.}$ of 19.5 %

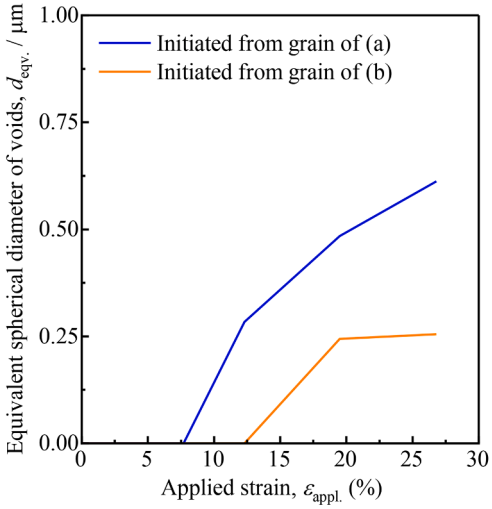

(c) Initiation and growth behavior of voids initiated from the γ phase grains shown in (a) and (b)

Fig. 9. Graphs show the 4D transformation behaviour of γ-phase grains where voids were initiated at an applied strain $\varepsilon_{appl.}$ of (a) 12.3% and (b) 19.5%. The dotted circles indicate the locations where the voids were initiated. (c) initiation and growth behaviour of voids that originated from the γ-phase grains shown in (a) and (b).

that the strength of the γ phase of the specimen is inferred from its chemical composition to be comparable to the material examined by Samek et al., the suppression of martensitic transformation described above is considered to be more dominant than the autocatalytic effect in the sample. In the present study, an increase in the local γ phase volume fraction was also found to inhibit the initiation and growth of voids. This effect can be reasonably understood when considering the three factors mentioned above: reduction in stress triaxiality, stress relaxation and the constraint of plastic deformation. These factors may also act effectively as mechanisms to inhibit void initiation and growth.

In addition to the macroscopic γ phase volume fraction, factors influencing the local γ phase volume fraction include the non-uniform distribution of γ-phase grains and their connectivity within the material matrix. In the present study, it has been shown that the surface irregularities and morphological complexity of the γ-phase grains influence the martensitic transformation and damage behaviour. This is also closely related to the connectivity of the γ-phase grains and will be discussed together in Section 4.2.

4.1.2. *Effect of the shape of γ-phase grains*

Tsuchida et al. evaluated the stability of TRIP steels using two types of steels with controlled microstructures, resulting in either lumpy or needle-like (i.e. lamella-like in 3D) γ-phase grains. It was concluded that the needle-like γ-phase grains exhibited higher stability [15]. Sugimoto et al. [45] compared networked, lumpy and needle-like γ-phase grains, and Chiang et al. [14] compared lumpy and needle-like γ-phase grains, with both studies reaching similar conclusions. The TRIP steels used in these studies compared samples with very distinct γ-phase grain geometries. The present study, on the other hand, evaluated the stability and susceptibility to damage of γ phases of different shapes in a single sample, aiming for more precise microstructural control. Therefore, the differences in alloying element concentrations per γ-phase grain are likely to be relatively small compared to the samples of Tsuchida et al. and Sugimoto et al. The present study clearly shows that simplistic classifications such as needle, plate and lump are not adequate for assessing the stability of the γ phase. Furthermore, no accelerated martensitic transformation or damage was observed even when the principal axis coincided with the tensile direction and internal stresses

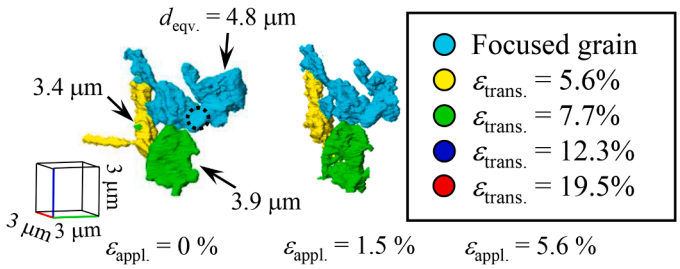

(a) γ phase grain with small surrounding γ phase grains

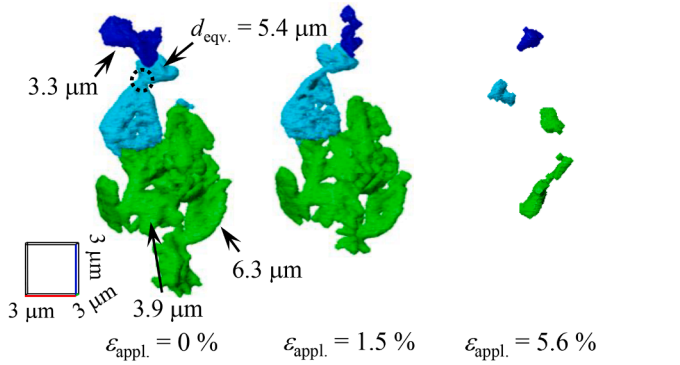

(b) γ phase grain with coarse surrounding γ phase grains

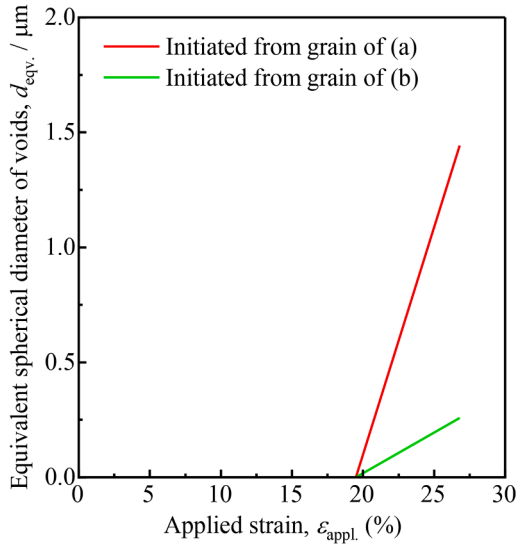

(c) Growth behavior of voids initiated in the γ phase grains shown in (a) and (b).

Fig. 10. Graphs show (a) and (b) transformation behaviour of γ-phase grains where voids were initiated at an applied strain, ε_{appl}, of 26.8%. The dotted circles indicate the locations where the voids were initiated; (c) changes in the equivalent spherical diameter of voids that originated from the γ-phase grains examined in (a) and (b).

appeared to be high. This may be due to the predominant effect of the local geometry of the γ-phase grains. Indeed, the martensitic transformation of individual γ-phase grains was observed to originate from areas with locally distorted geometry.

p_7, which was found in this study to be able to successfully control martensitic transformation and damage behaviour, is considered to be a parameter that expresses the local shape complexity, which influences martensitic transformation and damage behaviour. p_7 is a microstructural design variable that is sensitive to both martensitic transformation and subsequent damage behaviour, suggesting that the γ-phase grains that transform at an early stage are more prone to damage and can have a detrimental effect on the overall integrity of the material. Therefore, p_7 is considered a useful overall indicator of microstructural control in TRIP steels. On the other hand, p_8, which represents the skewness of the voxel distribution, was as sensitive to γ-phase grain stability as p_7, but less sensitive to damage. This is presumably because the presence of a small number of discontinuities, to which p_8 is sensitive, promotes martensitic transformation but does not necessarily reduce the fracture strength of the α′ phase grains due to their local shape and orientation.

In α′ phase grains with large p_7 values, plastic deformation of the surrounding γ-phase grains may be constrained in areas of locally distorted geometry, leading to a local increase in stress triaxiality. This promotes stress-assisted martensitic transformation in the early stages of deformation through increased mechanical driving forces, as discussed in Section 4.1. However, the effect of p_7 is only noticeable after an applied strain of 5.6%, and the effect of the high p_7 in the sample is thought to occur mainly during strain-induced martensitic transformation. Therefore, it is reasonable to assume that the presence of distorted parts in the geometry of the grains contributes to local transformation, which is driven by the increased inhomogeneity of deformation in both the α and γ phases.

4.1.3. *Effect of γ phase orientation*

Fig. 7(a) shows that the martensitic transformation of γ-phase grains of the intermediate crystallographic orientations is the slowest below 4% applied strain, especially up to 1.5%, which is the first loading stage. On the other hand, the martensitic transformation of γ-phase grains with ⟨110⟩ orientation was the fastest, being about four times faster than the transformation rate of γ-phase grains with intermediate crystallographic orientations. This may be related to the large mechanical driving force for stress-assisted transformation, as shown in Fig. 7(b). Yamashita et al. also found that γ-phase grains near ⟨100⟩ and ⟨110⟩ orientations rapidly undergo a martensitic transformation, while grains rotating towards $a <$ 111> orientation show the opposite behaviour [42]. This preferential orientation is attributed to the Kurdjumov–Sachs relation, with α-phase grains oriented in the ⟨100⟩ direction [42]; Tirumalasetty et al. [16] reported that γ phase grains surrounded by α-phase grains tend to undergo orientation rotation and that this rotation leads to retardation of martensitic transformation due to a reduction in the Schmidt factor after rotation. They measured an orientation rotation of up to 9.3° at an applied strain of only 1.1% [16]. However, in the sample used, as in the previous report [30], the crystallographic orientation rotation is small up to an applied strain of 5.6%, averaging around 2° This limited rotation is thought to be the reason for the strong dependence on initial orientations.

The γ-phase grains oriented in the ⟨111⟩ direction have a medium mechanical driving force for strain-induced transformation, and exhibit rapid transformation up to an applied strain of 5.6%, after which the transformation rate significantly slows down. In contrast, γ-phase grains oriented in the ⟨100⟩ direction complete their transformation early. No rotation of the γ-phase grains towards a specific crystallographic orientation was observed in the sample, even at medium to high levels of strain. Therefore, the orientation-dependent transformation behaviour at medium to high strains is probably due to the different dislocation densities, as shown in Fig. 7(c). γ-phase grains with $a <$ 100> orientation have a high initial dislocation density. Moreover, these grains experience a more pronounced rate of increase in dislocation density during deformation, reaching levels several times higher than that of γ-phase grains oriented in the ⟨111⟩ direction at an applied strain of 5.6%. Shear band intersections, which are nucleation sites for strain-induced martensitic transformation, are introduced by plastic deformation of the γ-phase grains. Therefore, the density of shear band intersections is expected to be higher in γ-phase grains oriented in the ⟨100⟩ direction [43,46,47].

Thus, the mechanism of martensitic transformation in materials, particularly in TRIP steels, and the factors controlling it differ between the initial and subsequent plastic deformation stages. The occurrence of

either stress-assisted or strain-induced martensitic transformation is influenced by a combination of factors, including temperature, the stress state of the material, its chemical composition and austenitisation conditions [48]. The striking curve shape in Fig. 7(a), which shows a reversal in the rate of martensitic transformation at an applied strain of about 4%, may reflect a switch between the two transformation mechanisms.

4.2. Material design indications

The formation of voids in materials not only leads to a reduction in mechanical properties such as strength and ductility but also to a deterioration in formability. In this study, it was found that the growth of preexisting voids formed during the manufacturing process is slow, and that it is important to control the voids formed in the early stages of plastic deformation. It was also found that almost all of the voids formed during deformation are formed in the transformed γ-phase grains and that controlling the γ-phase grains is key to controlling damage, particularly at the initial stage. It is known that less stable γ-phase grains do not improve ductility [13], and it is clear that controlling the stability of these grains is crucial [48]. In other words, it is desirable that martensitic transformation of the γ-phase grains occurs when necking occurs at higher applied strains, such as 20% applied strain for the material used, and that void formation is suppressed by the associated dilatational strain. Therefore, the damage resistance of the material used can be improved by increasing the stability of the γ-phase grains through the various microstructural controls described in the introduction.

It is known that high C concentration, small grain size, the presence of alloying elements such as Mn and Si, and stress conditions such as hydrostatic pressure are important for the stability of γ-phase grains [18]. The effects of these factors on the damage of γ-phase grains have also been reported. For example, Jacques et al. [8] have shown the mechanism by which the carbon concentration of γ-phase grains in TRIP steels affects damage formation. They proposed two primary mechanisms. One explanation is that the high carbon content in γ-phase grains leads to their transformation into high-strength α′-phase grains, resulting in greater strain incompatibility between α and α′ and promoting delamination. The other hypothesis is that the higher the carbon concentration, the more brittle the α' phase, making it more prone to fracture. It is also important to control the morphology and spatial distribution of the γ-phase grains because of the increase in internal stress in the preceding α′ grains and the plastic constraint imposed on the surrounding γ-phase grains. In other words, achieving uniformity and random distribution of γ-phase grain size is considered effective for damage prevention.

In the present study, the parameter p_7, representing the deviation of the voxel spatial distribution, showed high sensitivity to both martensitic transformation and subsequent damage behaviour in steel. p_7 is a microstructural design variable that expresses the complex shape characteristics of γ-phase grains, such as the presence of strong local stress concentrations. The γ phase grains investigated in this steel are derived from the reverse transformation of γ formed during annealing in the duplex region at 677 K. Therefore, the shape of these γ-phase grains is assumed to reflect the shape of the γ formed during this reverse transformation. In other words, γ-phase grains with a small p_7 are relatively small γ-phase grains that grew in isolation during reverse transformation, while γ-phase grains with a large p_7 are relatively small γ-phase grains that grew in close proximity to multiple γ-phase grains during reverse transformation. This suggests that γ-phase grains with various orientations are likely to form and partially bond with each other during the reverse transformation. According to Olson et al. [49], the slip deformation occurring in γ-phase grains plays a crucial role in suppressing the growth of α′ phase grains, resulting in their irregular shape. Uniform slip deformation is, therefore, considered to be important for controlling the local morphology of the γ-phase grains. It is also thought that the p_7 value will be smaller for grains that are isolated without other γ-phase grains around them at the time of reverse transformation. Conversely, γ-phase grains that have undergone significant growth after coalescing with neighbouring γ-phase grains are also likely to show a smaller p_7. In addition, the surface irregularities of the γ-phase grains correspond to the interface between the γ- and α-phase grains. Therefore, if the movement of the phase interface is suppressed during cooling after reverse transformation, a smoother surface condition on the γ-phase grains is expected to be achieved, resulting in a smaller p_7.

The crystalline orientation of the α phase cannot be measured in this study; the orientation relationship between the α and γ phases may have some influence on the transformation of the γ phase and subsequent void generation behaviour. However, given the high correlation between the factors considered in this study and the transformation and subsequent void generation behaviour of the γ phase, it is expected that the results would not change significantly even if the orientation relationship between the α and γ phases were measured and considered. This is due to the fact that the α' phase is much harder than the other two phases.

In the present study, p_7 was measured using a high-resolution imaging-type X-ray CT setup under synchrotron radiation. 3D measurements are essential to obtain p_7. Tirumalasetty et al. [16] compared the bulk surface and internal martensitic transformation behaviour by EBSD/XRD and reported significant differences. In addition, given the properties of the γ phase, which is susceptible to martensitic transformation, non-destructive 3D observation using X-ray CT and other methods is essential. The imaging-type X-ray CT used in this study has the highest spatial resolution among various X-ray CT systems for medical, industrial and academic research. However, its application is limited to third-generation or more advanced synchrotron radiation facilities and on beamlines equipped with insertion devices such as undulators. Similar high-resolution observations cannot be achieved with laboratory-scale X-ray CT systems. Therefore, it may be useful to utilise imaging-type X-ray CT to support routine synchrotron radiation production CT or lab-scale industrial X-ray CT observations, which have lower spatial resolutions. For example, the complex local shapes in the high-resolution 3D images, reflected by p_7, would be captured as subtle pixel value fluctuations in synchrotron projection X-ray CT or microfocus industrial X-ray CT systems. Therefore, it is expected that the control and management of various manufacturing parameters in industries and other sectors will become feasible if the pixel value fluctuations in 3D images captured with lower-spatial-resolution devices can be quantified and correlated with p_7.

5. Conclusion

A comprehensive multimodal measurement environment combining X-ray CT and pencil beam XRD has been developed and applied for the first time to stress-assisted and strain-induced martensitic transformation and damage behaviour in TRIP steels. This study analysed the martensitic transformation and damage behaviour of individual γ-phase grains in detail, including the interactions between neighbouring grains. The aim was to identify the factors controlling the transformation and damage behaviour of γ-phase grains and to derive insights for the architectural design of TRIP steel microstructures that show high resistance to damage.

The martensitic transformation of a substantial number of γ-phase grains commenced at low applied strains, and by the time the strain reached 5.6%, a significant number of these grains had undergone complete martensitic transformation. Initially, the transformation was primarily stress-induced, propelled by mechanical driving forces. γ-phase grains oriented in the ⟨110⟩ and ⟨100⟩ directions, which experienced high mechanical driving forces, transformed rapidly. A transition to a strain-induced martensitic transformation mechanism was then observed. With respect to the density of shear band intersections, which are the nucleation sites for strain-induced martensitic transformation, γ-phase grains oriented in the ⟨111⟩ direction, which had a high initial dislocation density, transformed most rapidly, whereas those oriented in

the ⟨110⟩ direction, with a slower increase in dislocation density, showed the slowest transformation rates, marking a characteristic inversion pattern. The influence of the preceding hard phase was threefold: it reduced stress triaxiality, facilitated stress relaxation and imposed constraints on plastic deformation, collectively inhibiting the martensitic transformation of the neighbouring γ-phase grains over a wide range of applied strains. It was also found that the influence of the shape of the γ-phase grains transcended the previously reported simplified geometries of needle, lump or plate. Instead, it was dominated by the local complex shapes and irregularities, as defined by the deviation (p_7) and skewness (p_8) parameters of the 3D pixel spatial distribution.

The growth of preexisting voids was slower, while new voids formed during the deformation process grew faster. Most of the voids formed during deformation originated from α′-phase grains after the transformation of the γ-phase grains. The voids that formed relatively early in the process grew significantly, making their control an important aspect of the process. p_7 was identified as highly sensitive in characterising the evolution of damage. This vulnerability is attributed to the presence of strong stress concentration zones in the α′ phase grains after the completion of the martensitic transformation. The study concludes that the initiation and progression of damage are determined by the superposition of interference effects between the shape of the γ-phase grains and the surrounding α′-phase grains.

Based on these findings, industrial measures for designing damage-resistant TRIP steels were investigated. Key considerations include controlling the shape of γ-phase grains using multiple 3D imaging apparatuses while using p_7 as an indicator for this process; ensuring a uniform dispersion of γ-phase grains throughout the steel; and increasing the stability of γ-phase grains.

Supplementary materials

The supplementary material associated with this article can be found, in the online version, at doi: XXXXXXXXX.

CRediT authorship contribution statement

Hiroyuki Toda: Writing – review & editing, Writing – original draft, Supervision, Project administration, Funding acquisition. **Chiharu Koga:** Writing – original draft, Visualization, Investigation, Formal analysis, Data curation. **Kyosuke Hirayama:** Writing – review & editing, Software, Investigation, Formal analysis. **Akihisa Takeuchi:** Writing – review & editing, Software, Resources. **Masayuki Uesugi:** Writing – review & editing, Software, Resources. **Kyohei Ishikawa:** Writing – review & editing, Resources. **Takafumi Yokoyama:** Writing – review & editing, Resources. **Hiro Fujihara:** Writing – review & editing, Visualization, Investigation, Formal analysis, Data curation.

Declaration of competing interest

The authors declare that they have no known competing financial interests or personal relationships that could have appeared to influence the work reported in this paper.

Acknowledgements

This work was partly supported by JSPS KAKENHI (grant numbers JP17H01328 and JP21H04624). The synchrotron experiments were performed with the approval of JASRI (proposal numbers 2021B1602, 2021A1470, 2022A1222, 2022B1158, 2023A1005 and 2023B1011).

Supplementary materials

Supplementary material associated with this article can be found, in the online version, at doi:10.1016/j.actamat.2024.120412.

References

[1] T. Maki, Current state and future prospects of microstructure control in steels, Tetsu-to-Hagane 81 (1995) N547–N555, in Japanese.
[2] S. Harjo, N. Tsuchida, J. Abe, W. Gong, Martensite phase stress and the strengthening mechanism in TRIP steel by neutron diffraction, Sci. Rep. 7 (2017) 15149.
[3] M. Grujicic, T. Erturk, W.S. Owen, A finite element analysis of the effect of the accomodation strains in the ferrite phase on the work hardening of a dual-phase steel, Mater. Sci. Eng. 82 (1986) 151–159.
[4] F.M. Al-Abbasi, J.A. Nemes, Micromechanical modeling of dual phase steels, Int. J. Mech. Sci. 45 (2003) 1449–1465.
[5] X. Sun, K.S. Choi, W.N. Liu, M.A. Khaleel, Predicting failure modes and ductility of dual phase steels using plastic strain localization, Int. J. Plast. 25 (2009) 1888–1909.
[6] E. Pereloma, A. Gazder, I. Timokhina, The transformation-induced plasticity effect and the stability of retained austenite in steels, in: R. Colás, G.E. Totten (Eds.), The Encyclopaedia of iron, Steel and Their Alloys, Taylor and Francis, New York, 2012.
[7] H.K.D.H. Bhadeshia, TRIP-Assisted Steels? ISIJ Int. 42 (2002) 1059–1060.
[8] P.J. Jacques, E. Girault, A. Mertens, B. Verlinden, J. van Humbeeck, F. Delannay, The developments of cold-rolled TRIP-assisted multiphase steels. Al-alloyed TRIP-assisted multiphase steels, ISIJ Int. 41 (2001) 1068–1074.
[9] S.O. Kruijver, L. Zhao, J. Sietsma, S.E. Offerman, N.H. van Dijk, E.M. Lauridsen, L. Margulies, S. Grigull, H.F. Poulsen, S. van der Zwaag, In situ observations on the mechanical stability of austenite in TRIP-steel, J. Phys. IV 104 (2003) 499–502.
[10] K.K. Park, S.T. Oh, S.M. Baeck, D.I. Kim, J.H. Han, H.N. Han, S.H. Park, C.G. Lee, S. J. Kim, K.H. Oh, In Situ Deformation Behavior of Retained Austenite in TRIP Steel, Mater. Sci. Forum 408-412 (2002) 571–576.
[11] E. Jimenez-Melero, N.H. van Dijk, L. Zhao, J. Sietsma, S.E. Offerman, J.P. Wright, S. van der Zwaag, Martensitic transformation of individual grains in low-alloyed TRIP steels, Scr. Mater. 56 (2007) 421–424.
[12] I.B. Timokhina, P.D. Hodgson, E.V. Pereloma, Effect of deformation schedule on the microstructure and mechanical properties of a thermomechanically processed C-Mn-Si transformation-induced plasticity steel, Metall. Mater. Trans. A 34 (2003) 1599–1609.
[13] S. Zhang, K.O. Findley, Quantitative assessment of the effects of microstructure on the stability of retained austenite in TRIP steels, Acta Mater. 61 (2013) 1895–1903.
[14] J. Chiang, B. Lawrence, J.D. Boyd, A.K. Pilkey, Effect of microstructure on retained austenite stability and work hardening of TRIP steels, Mater. Sci. Eng. A 528 (2011) 4516–4521.
[15] N. Tsuchida, T. Tanaka, Y. Toji, Analysis of tensile deformation behaviour by in situ neutron diffraction experiments of a 1 GPa-grade TRIP steel with high elongation, Tetsu-to-Hagane 105 (2019) 918–926, in Japanese.
[16] G.K. Tirumalasetty, M.A. van Huis, C. Kwakernaak, J. Sietsma, W.G. Sloof, H. W. Zandbergen, Deformation-induced austenite grain rotation and transformation in TRIP-assisted steel, Acta Mater. 60 (2012) 1311–1321.
[17] R. Blondé, E. Jimenez-Melero, L. Zhao, J.P. Wright, E. Bruck, S. van der Zwaag, N. H. van Dijk, Mechanical stability of individual austenite grains in TRIP steel studied by synchrotron X-ray diffraction during tensile loading, Mater. Sci. Eng. A 618 (2014) 280–287.
[18] L. Samek, E.D. Moor, J. Penning, B.C.D. Cooman, Influence of alloying elements on the kinetics of strain-induced martensitic nucleation in low-alloy, multiphase high-strength steels, Metall. Mater. Trans. A 37 (2006) 109–124.
[19] S. Kaar, K. Steineder, R. Schneider, D. Krizan, C. Sommitsch, New M_S-formula for exact microstructural prediction of modern 3 rdgeneration AHSS chemistries, Scr. Mater. 200 (2021) 113923.
[20] A. Gramlich, C. van der Linde, M. Ackermann, W. Bleck, Effect of molybdenum, aluminium and boron on the phase transformation in 4 wt .-% manganese steels, Result. Mater. 8 (2020) 100147.
[21] J. Mahieu, J. Maki, B.C. Cooman, S. Claessens, Phase transformation and mechanical properties of Si-free CMnAl transformation -induced plasticity-aided steel, Metall. Mater. Trans. A 33 (2002) 2573–2580.
[22] S.J. Lee, K.S. Park, Prediction of martensite start temperature in alloy steels with different grain sizes, Metall. Mater. Trans. A 44 (2013) 3423–3427.
[23] G.N. Haidemenopoulos, A.N. Vasilakos, Modelling of austenite stability in low-alloy triple-phase steels, Steel Res. 67 (1996) 513–519.
[24] A. Devaraj, Z. Xu, F. Abu-Farha, X. Sun, L.G. Hector Jr, Nanoscale solute partitioning and carbide precipitation in a multiphase TRIP steel analyzed by atom probe tomography, JOM 70 (2018) 1752–1757.
[25] H.W. Luo, J. Shi, C. Wang, W. Cao, Z. Sun, H. Dong, Experimental and numerical analysis on the formation of stable austenite during intercritical annealing of 5Mn steel, Acta Mater. 59 (2011) 4002–4014.
[26] J. Han, S.J. Lee, L.G. Jung, Y.K. Lee, The effects of the initial martensite microstructure on the microstructure and tensile properties of intercritically annealed Fe-9Mn-0.05C steel, Acta Mater. 78 (2014) 369–377.
[27] T. Nakagaito, H. Matsuda, Y. Nagataki, K. Seto, Effects of partitioning of manganese and silicon during intercritical annealing on transformation behaviour and mechanical properties of low alloyed TRIP-assisted Steel Sheets, Tetsu-to-Hagane 101 (2015) 426–434, in Japanese.
[28] O. Matsumura, Y. Sakuma, H. Takechi, Enhancement of elongation by retained austenite in intercritical annealed 0.4C-1.5Si-O.8Mn steel, Trans. isij 21 (1987) 570–579.
[29] M.L. Brandt, G.B. Olson, Bainitic Stabilization of Austenite in Low Alloy Sheet Steels, Iron Steelmak. 20 (1993) 55–60.
[30] H. Toda, K. Hirayama, K. Okamura, T. Suzuki, A. Takeuchi, M. Uesugi, H. Fujihara, Multimodal assessment of mechanically induced transformation in metastable

multi-phase steel using X-ray nano-tomography and pencil-beam diffraction tomography, Acta Mater. 234 (2022) 117956.
[31] H. Toda, C.T. X-Ray, Hardware and Software Techniques, Springer Nature Singapore, Singapore, 2021.
[32] H.F. Poulsen, An introduction to three-dimensional X-ray diffraction microscopy, J. Appl. Crystallogr. 45 (2012) 1084–1097.
[33] H. Toda, T. Kamiko, Y. Tanabe, M. Kobayashi, D.J. Leclere, K. Uesugi, A. Takeuchi, K. Hirayama, Diffraction-amalgamated grain boundary tracking for mapping 3D crystallographic orientation and strain fields during plastic deformation, Acta Mater. 107 (2016) 310–324.
[34] H. Toda, A. Takijiri, M. Azuma, S. Yabu, K. Hayashi, D. Seo, M. Kobayashi, K. Hirayama, A. Takeuchi, K. Uesugi, Damage micromechanisms in dual-phase steel investigated with combined phase- and absorption-contrast tomography, Acta Mater. 126 (2017) 401–412.
[35] C. Gupta, H. Toda, C. Schlacher, Y. Adachi, P. Mayr, C. Sommitsch, K. Uesugi, Y. Suzuki, A. Takeuchi, M. Kobayashi, Study of creep cavitation behaviour in tempered martensitic steel using synchrotron micro-tomography and serial sectioning techniques, Mater. Sci. Eng., A 564 (2013) 525–538.
[36] D. Bradley, G. Roth, Adaptive thresholding using the integral image, J. Graph. Tool. 12 (2007) 13–21.
[37] H. Toda, H. Li, R. Batres, K. Hirayama, H. Fujihara, Surrogate-based optimization of microstructural features of structural materials, Acta Mater. 257 (2023) 11918.
[38] B.D. Cullity, Elements of X-ray Diffraction, Addison-Wesley Educational Publishers Inc., Boston, USA, 1956.
[39] T. Ungár, S. Ott, P.G. Sanders, A. Borbély, J.R. Weertman, Dislocations, grain size and planar faults in nanostructured copper determined by high resolution X-ray diffraction and a new procedure of peak profile analysis, Acta Mater 46 (1998) 3693–3699.
[40] R. Blondé, E. Jimenez-Melero, L. Zhao, J.P. Wright, E. Brück, S. van der Zwaag, N. H. van Dijk, High-energy X-ray diffraction study on the temperature-dependent mechanical stability of retained austenite in low-alloyed TRIP steels, Acta Mater. 60 (2012) 565–577.
[41] G.N. Haidemenopoulos, M. Grujicic, G.B. Olson, M. Cohen, Thermodynamics-based alloy design criteria for austenite stabilization and transformation toughening in the Fe-Ni-Co system, J. Alloy. Compd. 220 (1995) 142–147.
[42] T. Yamashita, N. Koga, O. Umezawa, Martensitic transformation of retained austenite in ferrite matrix for low alloy steel, Mater. Trans. 59 (2018) 712–716.
[43] G.N. Haidemenopoulos, N. Aravas, I. Bellas, Kinetics of strain-induced transformation of dispersed austenite in low-alloy TRIP steels, Mater. Sci. Eng., A 615 (2014) 416–423.
[44] F. Lani, Q. Furnṁont, T. Van Rompaey, F. Delannay, P.J. Jacques, T. Pardoen, Multiscale mechanics of TRIP-assisted multiphase steels: II. micromechanical modelling, Acta Mater. 55 (2007) 3695–3705.
[45] K. Sugimoto, M. Misu, M. Kobayashi, H. Shirasawa, Effects of second phase morphology on retained austenite morphology and tensile properties in a trip-aided dual-phase steel sheet, ISIJ Int. 33 (1993) 775–782.
[46] P.J. Gibbs, E. De Moor, M.J. Merwin, B. Clausen, J.G. Speer, D.K. Matlock, Austenite stability effects on tensile behaviour of manganese-enriched-austenite transformation-induced plasticity steel, Metall. Mater. Trans. A 42 (2011) 3691–3702.
[47] A. Perlade, O. Bouaziz, Q. Furneṁont, A physically based model for TRIP-aided carbon steels behaviour, Mater. Sci. Eng., A 356 (2003) 145–152.
[48] K. Sugimoto, M. Kobayashi, S. Hashimoto, Ductility and strain-induced transformation in a high-strength transformation-induced plasticity-aided dual-phase steel, Metall. Mater. Trans. A 23 (1992) 3085–3091.
[49] G.B. Olson, M. Azrin, Transformation behavior of TRIP steels, Metall. Trans. A 9 (1978) 713–721.